A Multienergy Interface Electric-Drive-Reconstructed Onboard Charger for EVs With Integrated Control Strategy

Feng Yu, *Member, IEEE*, Qihao Yin, Zhihao Zhu, and Xunhui Cheng

***Abstract*—In this article, an innovative multienergy interface electric-drive-reconstructed onboard charger (MEI-EDROC) and its derivative integrated control strategy (ICS) are proposed for a solar-powered electric vehicle that is equipped with a six-phase machine drive. The proposed MEI-EDROC is capable of dc charging, single-phase charging, in-motion charging, and normal driving with applications for single-phase ac grid, dc grid, and photovoltaic energy input interfaces. In particular, all the operation modes are implemented by the ICS extended from the vector control of the six-phase permanent-magnet synchronous machine. First, the topology and operation modes of the proposed MEI-EDROC are discussed. Then, operation principles for all work scenarios are studied in detail, and the concept of integrated control is proposed. Thereafter, based on the vector control strategy, the ICS is designed. Finally, a 2-kW experimental test rig is built, and the obtained results verify the steady-state and dynamic performances, as well as the mode switching operation.**

***Index Terms*—Electric-drive-reconstructed onboard charger (EDROC), integrated control strategy (ICS), multienergy interface, six-phase machine drive, solar-powered electric vehicle (SPEV).**

I. Introduction

With the ever-increasing concern for environmental problems, electric vehicles (EVs) have recently attracted a great deal of attention for transportation, and many advances have been made in EVs. However, the unsatisfactory mileage range and the inconvenience of charging are still the main obstacles to further popularizing EVs, at the present status of the limited battery energy density and the relatively low geographical density of high-power fast EVs charging station (piles) [1].

Manuscript received 3 September 2023; revised 10 November 2023; accepted 21 December 2023. Date of publication 1 January 2024; date of current version 16 February 2024. The work was supported in part by the National Natural Science Foundation of China under Grant 52177051, and in part by the Excellent Young Backbone Teacher of "Qinglan Project" of Jiangsu Colleges and Universities (2022). Recommended for publication by Associate Editor R. Zane. *(Corresponding author: Feng Yu.)*

Feng Yu, Qihao Yin, and Xunhui Cheng are with the School of Electrical Engineering, Nantong University, Nantong 226019, China (e-mail: yufeng628@ntu.edu.cn; 2212310015@stmail.ntu.edu.cn; cheng@stmail.ntu.edu.cn).

Zhihao Zhu is with the School of Electrical and Information Engineering, Tianjin University, Tianjin 300018, China (e-mail: zhihao_zhu@tju.edu.cn).

Color versions of one or more figures in this article are available at https://doi.org/10.1109/TPEL.2023.3348822.

Digital Object Identifier 10.1109/TPEL.2023.3348822

As a tradeoff between cost, weight, volume, and charging power, the onboard charger (OBC) has been employed as a supplement over the charging station (pile) [1]. In particular, due to the lower cost, higher power level, and almost negligible increase in volume and weight compared with the additionally mounted OBC, electric-drive-reconstructed onboard charger (EDROC) has been studied in many aspects during the last few decades, including topologies, torque elimination, and performance improvement [2], [3], [4].

A single-phase EDROC topology based on a three-phase drive system was initially proposed in 1985 [5]. After that, single-phase, three-phase, and dc EDROC topologies in conjunction with different three-phase machines such as induction machine, permanent-magnet synchronous machine (PMSM), and switched reluctance machine, are studied one after another [6], [7]. Moreover, the multiphase machine is a promising candidate for EV applications owing to the smooth torque production, extra control degrees of freedom, and the inherent fault-tolerant capability [8], [9]. Hence, a great deal of single-phase and three-phase EDROC topologies based on five-phase, six-phase, and nine-phase machines are reported successively [10], [11], [12]. In addition, EVs must remain strictly stationary during charging so that the electromagnetic torque production should be analyzed in charging states. In [13] and [14], on the basis of the magnetic coenergy, the relationship between the machine rotor position and the charging electromagnetic torque is studied in detail for single-phase and three-phase EDROCs, respectively. In [15], a torque-free EDROC unified criterion is introduced to improve the generality of the EDROC. Furthermore, an additional high-frequency inductor is installed between the neutral point of the three-phase machine windings and the battery in [16], which effectively reduces the ripple of machine winding current, and hence, mitigates the machine vibration and the resulting noise. Besides, a method for reducing machine iron and semiconductor losses is discussed in [17], while a detailed efficiency calculation method is introduced and certified by experiments. Moreover, in [18], for the sake of ensuring normal operations in faulty cases, the postfault charging operation of an EDROC integrated by a nine-phase drive is studied exhaustively.

Apart from the aforementioned EDROCs powered by single-phase, three phase and dc grids, the one supplied by vehicle-roof photovoltaic panels (VRPPs) has drawn tremendous research

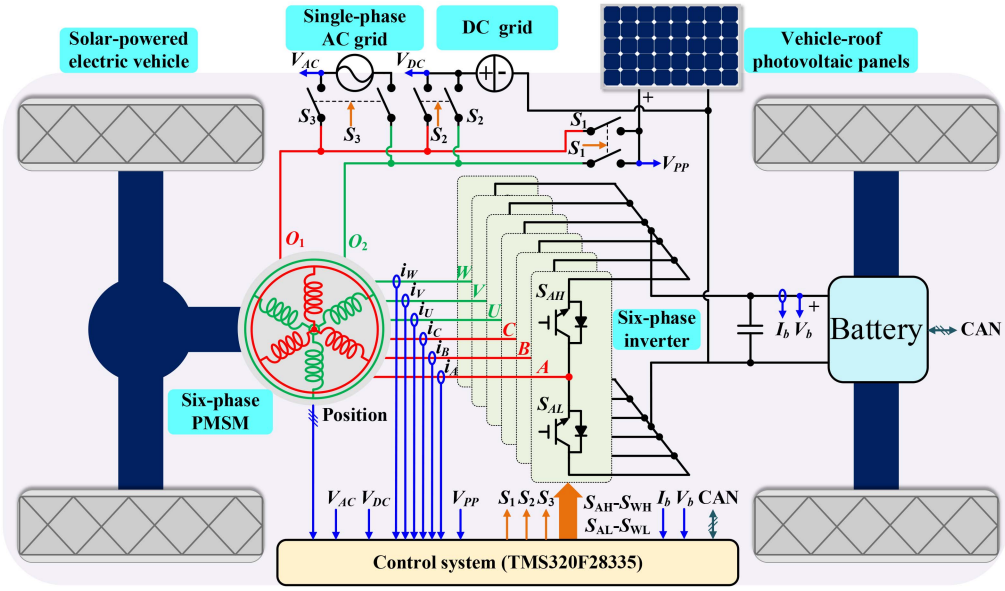

Fig. 1. Proposed topology of the MEI-EDROC.

interest for solar-powered EVs (SPEVs), which are more environmentally friendly and mileage-range-enhanced [19], [20]. As an example, the SPEV called "Lightyear One" designed by Lightyear company can averagely extend 12 km of range in one hour by the energy generated from its VRPPs [21], without any cost. Combined with this type of EVs, a dc EDROC is proposed in [22], where the battery pack can be charged by the VRPPs during driving, further extending the mileage range. However, a half H-bridge power module needs to be added. To address this drawback, an EDROC based on a six-phase drive is studied in [23], where the output power of VRPPs can be adjusted by the 0_1-axis current, without hardware added.

Notwithstanding that the aforementioned EDROCs cleverly avoid the demerits of the traditional EV chargers, and some among them can enlarge the EV mileage range to a certain extent, there are still two improving points for the recent EDROCs. First, in order for maximum facilitation of charging, EDROCs should have both dc and ac charging capabilities, while the recent EDROCs only take one of them. In particular, the in-motion charging (charging and driving simultaneously) function should be equipped for SPEVs, to enhance the utilization of VRPPs. Although the topology proposed in [24] provides the dc charging, ac charging, and in-motion charging functions, the machine will tremble in the ac charging mode and the circuit structure has to be frequently modified according to the load in the in-motion charging mode. Then, the control strategies for driving and charging are usually designed separately, thus increasing the design cost and control complexity. Besides, in regard to EDROCs in [22] and [23], the working control strategy inevitably alters between the in-motion charging and the dc charging modes because of the frequently switched going-stopping states of SPEVs. Essentially, battery charging is implemented by regulating the 0-axis current in the topologies proposed in [15], [16], [22], and [23], which implies the possibility of integrating the charging and the driving control strategies together.

In this article, an innovative multienergy interface EDROC (MEI-EDROC) and the derivative integrated control strategy (ICS) are proposed for the SPEV equipped with a six-phase drive, as shown in Fig. 1. The topology artfully takes the functions of dc charging, single-phase charging, in-motion charging, and normal driving. In terms of the studied MEI-EDROC, three main merits are indicated as follows.

1) Only three mode switches and three voltage sensors are extra mounted, compared to a standard six-phase drive system, and the VRPPs are integrated into the system without an additional dc/dc converter. Thus, the whole structure has no change for all operation modes, indicating that the charger is cheaper, smaller, and more reliable.
2) The MEI-EDROC can be supplied by a single-phase ac grid, emerging dc grid, and VRPPs, leading to a higher convenience for EV charging.
3) In view of the control perspective, the ICS is simpler and more reliable than the control strategies dedicated to the existing EDROCs.

The rest of this article is organized as follows. First, the operation modes of the studied MEI-EDROC are discussed in Section II. Second, operating principles for all work scenarios are studied exhaustively. After that, the concept of integrated control is proposed in Section III. Third, the ICS is designed in Section IV. Then, to verify the steady state and dynamic behavior of the proposed MEI-EDROC system under different operation scenarios, a 2-kW experimental test rig based on tests has been conducted in Section V. Finally, Section VI concludes this article.

II. Topology and Operation Modes Analysis

A. Topology and Operating Modes

The studied MEI-EDROC is composed of a six-phase PMSM with two available neutral points, a battery, a six-phase two-level

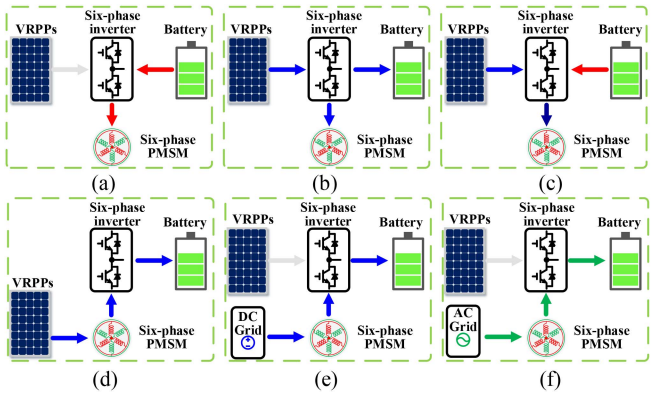

Fig. 2. Working states of the proposed MEI-EDROC. (a) State 1. (b) State 2. (c) State 3. (d) State 4. (e) State 5. (f) State 6.

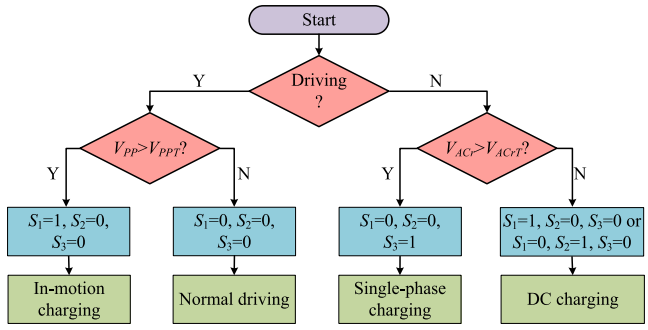

Fig. 3. Flow chart for mode switching and operating modes.

inverter, a set of VRPPs, a digital control system, three extra mode switches (S_1, S_2, S_3), and three extra voltage sensors (measuring $V_{\rm AC}$, $V_{\rm DC}$, and $V_{\rm PP}$), as shown in Fig. 1. The system can access to three energy input interfaces: single-phase ac grid, dc grid, and VRPPs. According to the EV operation state, the corresponding input energy interface is connected by controlling mode switches S_1, S_2, and S_3, and six working states are supported, as illustrated in Fig. 2. In addition, the flow chart for mode switching and operating modes of the system is presented in Fig. 3, for the sake of a clear presentation. First, it is mandatory to identify the EV operation state, either in driving or idle state. Subsequently, the VRPPs output voltage $V_{\rm PP}$ (when EV is in driving state) or the voltage rms value of the single-phase ac grid interface $V_{\rm ACr}$ (when EV is in idle state) is determined. Finally, the corresponding mode switch is closed and the system runs in the relevant mode.

In the case of the driving state, if $V_{\rm PP}$ is bigger than its set threshold voltage $V_{\rm PPT}$, the mode switch S_1 will be closed and the system will operate in the in-motion charging mode; otherwise, all mode switches are opened and the normal driving mode is active. During the idle state, while $V_{\rm ACr}$ is larger over its set threshold voltage $V_{\rm ACrT}$, the mode switch S_3 will be in ON and the single-phase ac charging mode will be employed. Moreover, the system would run in the dc charging mode in two switching states. For one state, the mode switch S_1 is closed, and the VRPPs are connected to the system when $V_{\rm PP} > V_{\rm PPT}$. On the other state, the mode switch S_2 is closed when the $V_{\rm DC}$ is larger over its set threshold voltage $V_{\rm DCT}$ and the dc grid is employed. Here, threshold voltages $V_{\rm ACrT}$, $V_{\rm DCT}$, and $V_{\rm PPT}$ are only used to distinguish whether the single-phase grid and the dc grid are connected and whether the output power of VRPPs is large enough. Besides, it should be mentioned that the three-phase ac charging is not designed since the three-phase ac grid is generally used in industry and uncommon in residential and other public places.

B. Operation Mode Analysis

In this section, the four modes of operation shown in Fig. 3 are analyzed in detail, as follows.

1) *Normal driving mode:* In this mode, all energy input interfaces are disabled. The system operates in state 1 (see Fig. 2(a)) where the six-phase inverter is employed to drive the six-phase PMSM and all energy is supplied by the battery.
2) *In-motion charging mode:* In the in-motion charging mode, the VRPPs are connected between the machine natural points and the battery negative electrode. The six-phase inverter serves as both the driver of the machine and the regulator of maximum power point tracking (MPPT) operation for the VRPPs. In addition, the current outputted from VRPPs is evenly injected into the six machine windings to generate zero electromagnetic torque. Furthermore, the battery can be used as either a source or a load, which is contingent on the power generation of VRPPs. Considering the weather variation, the voltage and current changes of the VRPPs are dynamic during the in-motion charging mode. Therefore, according to the EV working conditions, the system can run on either state 2 (see Fig. 2(b), the battery is a load) under abundant illumination conditions or state 3 (see Fig. 2(c), the battery is a source) under insufficient illumination conditions. Furthermore, the power generated by the VRPPs is responsible not only for driving but for charging the battery as well.
3) *DC charging mode:* Regarding this mode, the mode switch S_1 or S_2 is closed, either state 4 for connecting VRPPs or state 5 for connecting the dc grid is employed as presented in Fig. 2(d) or (e). The six-phase inverter, in conjunction with the six-phase PMSM, is utilized as a Boost converter to regulate the VRPPs voltage (considering the MPPT operation) or the dc grid voltage to the charging level. The simplified system circuit in this mode is shown in Fig. 4(a), where $X \in \{A, B, C, U, V, W\}$ and the dc source can be either the dc grid or the VRPPs.
4) *Single-phase charging mode:* In this mode, the system operates in state 6 and the single-phase grid is connected between the two natural points. The six-phase drive is reconstructed as a triple-parallel single-phase H-bridge rectifier and its simplified system circuit can be depicted as Fig. 4(b), where $Y \in \{A, B, C\}$ and $Z \in \{U, V, W\}$. The single-phase grid voltage is rectified and adjusted by the H-bridge rectifier to charge the battery.

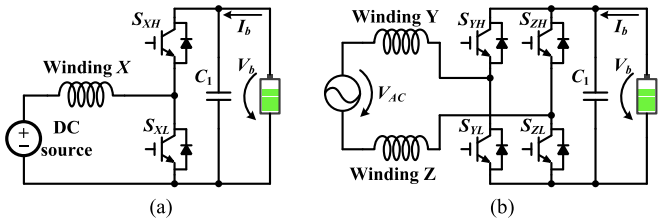

Fig. 4. (a) Simplified system circuit in DC charging mode. (b) Simplified system circuit in single-phase charging mode.

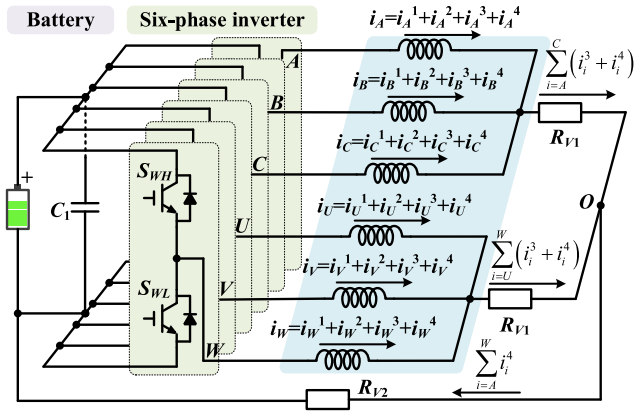

Fig. 5. Equivalent system circuit of the studied MEI-EDROC.

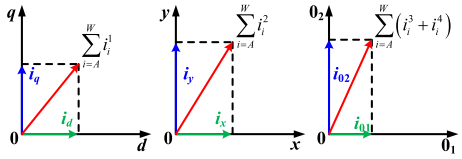

Fig. 6. Currents map.

III. Operation Principle

For the proposed MEI-EDROC, the system equivalent circuit is shown in Fig. 5, where I_X ($X \in \{A, B, C, U, V, W\}$) is the X-phase phase current. The phase current can be decoupled into four components ($I_X^1 - -I_X^4$) by the decoupling matrix $\mathbf{T}_1$ and the Park transformation $\mathbf{T}_{\text{park}}$. The currents with superscript "1," "2," "3," and "4" are mapped into d–q subspace, x–y subspace, 0_1-axis, and 0_2-axis, respectively, as shown in Fig. 6; and R_{V1} and R_{V2} are the equivalent impedances of circuit line.

$$\mathbf{T}_1 = \frac{1}{3}\left[\begin{array}{cccccc|c} 1 & 1/2 & -1/2 & -1 & -1/2 & 1/2 & \alpha \\ 0 & \sqrt{3}/2 & \sqrt{3}/2 & 0 & -\sqrt{3}/2 & -\sqrt{3}/2 & \beta \\ 1 & -1/2 & -1/2 & 1 & -1/2 & -1/2 & x \\ 0 & \sqrt{3}/2 & -\sqrt{3}/2 & 0 & \sqrt{3}/2 & -\sqrt{3}/2 & y \\ 1/2 & -1/2 & 1/2 & -1/2 & 1/2 & -1/2 & 0_1 \\ 1/2 & 1/2 & 1/2 & 1/2 & 1/2 & 1/2 & 0_2 \end{array}\right] \tag{1}$$

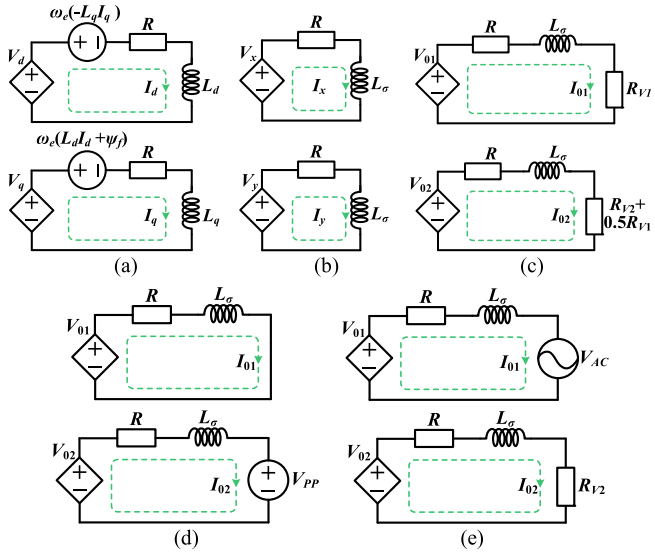

Fig. 7. Equivalent circuits for the MEI-EDROC. (a) Equivalent circuits in the d–q subspace. (b) Equivalent circuits in the x–y subspace. (c) 0_1- and 0_2-axes equivalent circuits in normal driving state. (d) 0_1- and 0_2-axes equivalent circuits in in-motion charging state or DC charging state. (e) 0_1- and 0_2-axes equivalent circuits in single-phase charging state.

$$\mathbf{T}_{\text{Park}} = \left[\begin{array}{cc} \cos\theta_e & \sin\theta_e \\ -\sin\theta_e & \cos\theta_e \end{array}\right] \begin{array}{|c} d \\ q \end{array} \tag{2}$$

where θ_e signifies the electrical angular.

A. Operation Principle of Normal Driving Mode

In the normal driving mode, the two neutral points of the six-phase PMSM are separated from each other and no source is connected between point O and the negative of the battery.

Hence, the values of equivalent impedances R_{V1} and R_{V2} are infinite. The equivalent circuit model after vector space decoupling and Park transformations can be drawn as in Fig. 7(a)–(c), and corresponding voltages can be presented as

$$\begin{bmatrix} V_d \\ V_q \end{bmatrix} = R\begin{bmatrix} I_d \\ I_q \end{bmatrix} + \begin{bmatrix} L_d & 0 \\ 0 & L_q \end{bmatrix}\frac{d}{dt}\begin{bmatrix} I_d \\ I_q \end{bmatrix} + \omega_e \begin{bmatrix} -L_q I_q \\ L_d I_d + \psi_f \end{bmatrix} \tag{3}$$

$$\begin{bmatrix} V_x \\ V_y \end{bmatrix} = R\begin{bmatrix} I_x \\ I_y \end{bmatrix} + L_\sigma \frac{d}{dt}\begin{bmatrix} I_x \\ I_y \end{bmatrix} \tag{4}$$

$$\begin{bmatrix} V_{01} \\ V_{02} \end{bmatrix} = \begin{bmatrix} R + R_{V1} & 0 \\ 0 & R + R_{V1}/2 + R_{V2} \end{bmatrix}\begin{bmatrix} I_{01} \\ I_{02} \end{bmatrix} + L_\sigma \frac{d}{dt}\begin{bmatrix} I_{01} \\ I_{02} \end{bmatrix} \tag{5}$$

where subscript "n" ($n \in \{d, q, x, y, 01, 02\}$) signifies that the variable is on the n-axis; L_d, L_q, and L_σ are the d-axis, the q-axis, and the stator leakage inductances, respectively; R is the stator resistance; ω_e is the electrical angular speed; and ψ_f is the permanent-magnet flux. With the decoupled machine model, the electromagnetic torque can be calculated as

$$T_e = 3p_n I_q \left(I_d \left(L_d - L_q\right) + \psi_f\right) \tag{6}$$

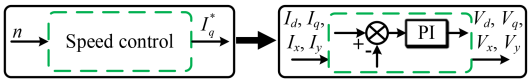

Fig. 8. Traditional control method for the six-phase PMSM drive.

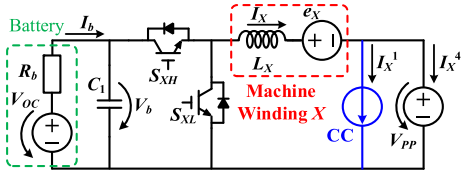

Fig. 9. Equivalent simplified circuit in the in-motion charging mode.

where p_n is the number of pole pairs. Thus, the output torque of the six-phase PMSM can be adjusted by controlling d–q subspace currents, which means that the speed can be regulated through d–q subspace currents. In other words, the six-phase PMSM drive is usually achieved by means of a speed controller, the d–q subspace current controller and the x–y subspace current controller, as shown in Fig. 8. Moreover, due to the infinite R_{V1} and R_{V2}, it has $I_{01} = 0$ and $I_{02} = 0$. It is unnecessary to adjust I_{01} and I_{02} in this mode.

B. Operation Principle of the in-Motion Charging Mode

When the VRPPs are connected between the neutral points and the battery negative point, $R_{V1} = 0$ and R_{V2} is replaced by a dc source. In this scenario, the d–q subspace and x–y subspace equivalent circuits are unaltered, whereas the 0_1- and 0_2-axes equivalent circuits change from Fig. 7(c) to (d). The 0_1- and 0_2-axes voltages can be expressed as

$$\begin{bmatrix} V_{01} \\ V_{02} \end{bmatrix} = R \begin{bmatrix} I_{01} \\ I_{02} \end{bmatrix} + L_\sigma \frac{d}{dt} \begin{bmatrix} I_{01} \\ I_{02} \end{bmatrix} + \begin{bmatrix} 0 \\ V_{\mathrm{PP}} \end{bmatrix}. \tag{7}$$

The variables of the d–q subspace, the x–y subspace, the 0_1-axis, and the 0_2-axis are decoupled mutually and can be controlled independently. On the basis of decoupling, the output power of VRPPs can be regulated by the 0_2-axis current to realize the MPPT purpose. The driving performance of the system can be regulated by controlling the d–q subspace currents, which are unrelated to the 0_2-axis current control. Besides, the output current of the VRPPs is equal to minus six times of the 0_2-axis current in this mode.

Without loss of generality, it is reasonable to only analyze one of the six phases (e.g., $X \in \{\mathrm{A}, \mathrm{B}, \mathrm{C}, \mathrm{U}, \mathrm{V}, \mathrm{W}\}$), as described in Fig. 9, where the stator resistance R is omitted. The battery can be equivalent to a resistor (R_b) connected with a voltage source (V_{OC}) in series. R_b is equivalent to the internal resistance of the battery and V_{OC} is the same as the battery open-circuit voltage associated with the battery state of charge [25]. Thus, the following equation can be obtained:

$$V_{\mathrm{OC}} - R_b I_b = V_b. \tag{8}$$

This equation indicates that the charge and discharge of the battery can be controlled by regulating V_b. The CC is I_X^1 current

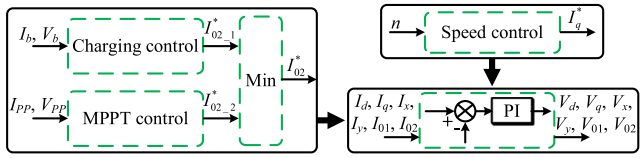

Fig. 10. Control method for in-motion charging.

loop component constructed by other phases of the six-phase drive system. I_X^1 is the d–q subspace part of I_X current, and I_X^4 is the 0_2-axis part of the I_X current in Fig. 9. Besides, x–y subspace and 0_1-axis currents are set to 0, which means $I_X^2 = I_X^3 = 0$ and they are not considered in the steady state. Thus, the change of I_X in one switch period related to the electrical angular θ_e can be expressed as

$$\begin{aligned} \Delta I_X &= \frac{t_1}{L_X}(V_b - V_{\mathrm{PP}} - e_X) + \frac{t_2}{L_X}(-V_{\mathrm{PP}} - e_X) \\ &= \frac{t_1}{L_X} V_b - \frac{T_s}{L_X}(V_{\mathrm{PP}} + e_X) \end{aligned} \tag{9}$$

where e_X is the electromotive force generated by rotor permanent magnets in the X-phase winding; L_X is the X-phase winding equivalent inductance; $T_s = t_1 + t_2$ is the switching period; t_1 and t_2 are the turn-ON and turn-OFF time of S_{XH}, respectively. It is worth highlighting that the current I_X^4 has no contribution to e_X as the magnetic field produced by the 0_2-axis current is zero. Thus, t_1 remains unaffected when the value of I_X^4 is increased or decreased by a constant amount. Furthermore, according to (9), a proportional change of t_1 will appear when V_{PP} changes, regardless of θ_e. The battery current I_{b} can be calculated as

$$\begin{aligned} I_b &= \frac{p_n \omega_m}{2\pi} \int_{t_0}^{t_0 + \frac{2\pi}{p_n \omega_m}} \frac{t_1}{T_s} I_X \, dt \\ &= \frac{p_n \omega_m}{2\pi} \int_{t_0}^{t_0 + \frac{2\pi}{p_n \omega_m}} \frac{t_1}{T_s} I_X^1 \, dt + \frac{p_n \omega_m}{2\pi} \int_{t_0}^{t_0 + \frac{2\pi}{p_n \omega_m}} \frac{t_1}{T_s} I_X^4 \, dt \end{aligned} \tag{10}$$

where t_0 is the start time of integration, and ω_m is the mechanical angular velocity. According to (10), if I_X^4 reduces, i.e., VRPPs output current increases, and I_b will drop. In addition, while V_{PP} rises, a constant value Δt_1 will be superimposed on t_1. As the I_X^1 is sinusoidal in steady state, Δt_1 has no effect on the first item of I_b. However, the second item of I_b will be smaller, since I_X^4 is less than zero. In conclusion, if VRPPs output current or voltage increases (or VRPPs output power increases), V_b will increase, and thus, the battery output current will drop. The control method for the in-motion charging mode is presented in Fig. 10.

Compared with the machine drive control method, charging control and MPPT control are added to achieve the purposes of battery-safe charging and the maximum power output of VRPPs, respectively. Furthermore, two extra control loops are arranged to regulate the 0_1- and 0_2-axes currents. It is pertinent to mention that the 0_2-axis current control is responsible for the MPPT operation of the VRPPs, as such, the dedicated dc–dc converter between the VRPPs and the battery is eliminated. Consequently,

TABLE I
DC CHARGING AND SINGLE-PHASE CHARGING CONTROL METHODS

Operation mode	Traditional control method	Proposed control method
DC charging mode (state 4)	I_{PV}, V_{PV} MPPT control I^*_{p1}; I_b, V_b Charging control I^*_{p2}; $I_A, I_B, \ldots I_W$ PI $V_A, V_B, \ldots V_y$	I_{PV}, V_{PV} MPPT control $I^*_{02\_2}$; I_b, V_b Charging control $I^*_{02\_1}$; $I_d, I_q, I_x, I_y, I_{01}, I_{02}$ PI $V_d, V_q, V_x, V_y, V_{01}, V_{02}$
DC charging mode (state 5)	I_b, V_b Charging control I^*_p; $I_A, I_B, \ldots I_W$ PI $V_A, V_B, \ldots V_y$	I_b, V_b Charging control I^*_{02}; $I_d, I_q, I_x, I_y, I_{01}, I_{02}$ PI $V_d, V_q, V_x, V_y, V_{01}, V_{02}$
Single-phase charging mode (state 6)	I_b, V_b, V_{AC} Charging control I^*_p; $I_A, I_B, \ldots I_W$ PIR $V_A, V_B, \ldots V_y$	I_b, V_b, V_{AC} Charging control I^*_{01}; I_d, I_q, I_x, I_y PI V_d, V_q, V_x, V_y; I_{01} PIR V_{01}

the designing cost of the system software and hardware can be decreased.

C. Operation Principle of the DC Charging Mode

In the dc charging mode, the 0_1- and 0_2-axes equivalent circuits are the same as in the in-motion charging mode. The system has two states: state 4 (the VRPPs are connected) and state 5 (the dc grid is connected), and in this case, $R_{V1} = 0$ and R_{V2} is replaced by a dc source. Currently, the six-phase drive system is simplified as a Boost converter, utilizing charging control and current control methods, as presented in Table I. The PI controller is employed to regulate all winding currents to the same value. However, the proposed control method generates zero electromagnetic torque in the motor by controlling the *d–q* and *x–y* subspace currents while controlling 0_2-axis current to regulate the charging power of the battery, the equivalent circuit model can be shown in Fig. 7(d). Essentially, 0_2-axis current is adjusted to charge the battery (and achieve MPPT when VRPPs are used). Consequently, it is feasible that *d–q*, *x–y*, 0_1-axis, and 0_2-axis current controls are applied to implement dc charging as shown in Table I.

D. Operation Principle of Single-Phase Charging Mode

Different from the dc charging mode, the single-phase grid is connected between the neutral points of the machine in this mode. R_{V1} can be replaced by a single-phase source and R_{V2} is infinite. Thus, the 0_1- and 0_2-axes equivalent circuits can be redrawn, as shown in Fig. 7(e) and the 0_1- and 0_2-axes voltage can be expressed as

$$\begin{bmatrix} V_{01} \\ V_{02} \end{bmatrix} = \begin{bmatrix} R & 0 \\ 0 & R + R_{V2} \end{bmatrix} \begin{bmatrix} I_{01} \\ I_{02} \end{bmatrix} + L_\sigma \frac{d}{dt} \begin{bmatrix} I_{01} \\ I_{02} \end{bmatrix} + \begin{bmatrix} V_{\mathrm{AC}} \\ 0 \end{bmatrix}. \tag{11}$$

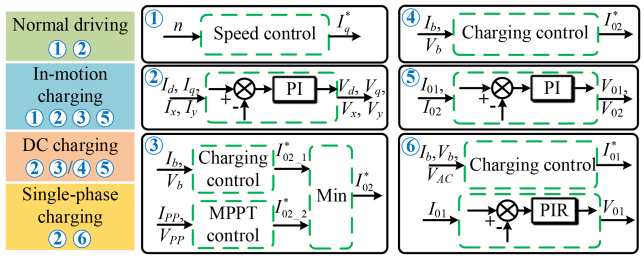

Fig. 11. Integrated control method for the EDROC.

As shown in Table I, the six-phase drive system is traditionally controlled as a triple parallel H-bridge rectifier. However, the output current of the single-phase grid can be adjusted by the 0_1-axis current loop. At the same time, *d–q* and *x–y* subspace current loops are employed to balance phase winding currents and keep EV stationary.

E. Integrated Control for the EDROC

According to the control method described in previous sections, the other three operation modes of the proposed MEI-EDROC can be carried out by extending the control of normal driving, as shown in Fig. 11. Considering the multicontrol degrees of freedom in multiphase drives, the charging voltage/current control can be converted into zero-sequence subspace current control. Hence, the integrated control concept is originally proposed and is implemented as follows.

First, *d–q* subspace current control loops are applied to regulate the machine speed. Meanwhile, they are also used to make the phase currents equal during the idle state of EVs. Second, *x–y* subspace current control loops are adopted to improve drive performance in both the normal driving mode and the in-motion charging mode. Besides, these two control loops contribute to balancing phase winding currents. Third, although 0_1- and 0_2-axes current control loops have no effect in the normal driving mode, the 0_1-axis current control loop is employed to regulate the charging current and realize power factor correction in the single-phase charging mode (the grid current is equal to minus three times 0_1-axis current). In addition, 0_2-axis current loop is responsible for the MPPT operation of VRPPs and adjusts the charging current in the in-motion mode and the dc charging mode (the output current VRPPs is equal to minus six times 0_2-axis current). Finally, the *d–q*, *x–y*, 0_1-axis, and 0_2-axis currents of the proposed MEI-EDROC are adjusted according to the given values in different modes, ultimately achieving control over various operating modes.

IV. CONTROLLER DESIGN

The proposed ICS shared for all operating modes is depicted in Fig. 12. The control diagram is mainly structured of seven components, namely decoupling transformation, speed control, reference values of 0_1- and 0_2-axes currents calculation, mode selection, machine currents control, inverse decoupling transformation, and pulsewidth modulation (PWM) generation. The ICS is implemented with the following steps.

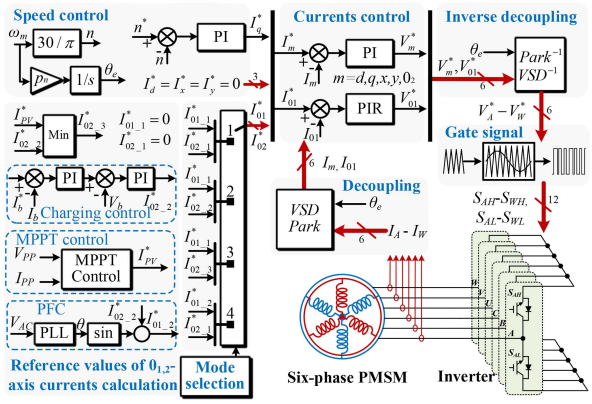

Fig. 12. Block diagram of the ICS.

1) First, the collected machine phase currents are decoupled from the ABC-UVW stationary coordinate to the *d*–*q* subspace, *x*–*y* subspace, 0_1-axis, and 0_2-axis by decoupling matrix $\mathbf{T}_1$ and the Park transformation matrix $\mathbf{T}_{\text{park}}$ (decoupling transformation).
2) Speed control is carried out by a PI controller to track the desired speed n^* in the normal driving and the in-motion charging modes while maintaining EV stationary in the dc charging and the single-phase charging modes ($n^* = 0$). Additionally, the *q*-axis current reference I_q^* is given by this PI controller and 0 is assigned to *d*-, *x*-, and *y*-axes current reference values.
3) The reference values of 0_1- and 0_2-axis currents are calculated in cases of dc grid, single-phase grid, VRPPs, and no source (i.e., without using grid or VRPPs) are connected, respectively, and those will be discussed in detail in the following part (see Section IV-A).
4) The operating modes of the MEI-EDROC are implemented by mode selection and the corresponding mode switch is closed. Meanwhile, the current reference values of the 0_1- and 0_2-axes for the relevant mode are employed, which will be discussed in the following part (see Section IV-B).
5) Then, the machine currents are regulated by five PI controllers and a proportional-integral-resonance (PIR) controller [3]. Here, the PIR controller is utilized to adjust the 0_1-axis current due to its sinusoidal reference value in the single-phase charging mode, which cannot be handled well by the bandwidth-limited PI controller.
6) V_d, V_q, V_x, V_y, V_{01}, and V_{02} are converted to ABC-UVW stationary coordinates by inverse decoupling transformation.
7) Finally, the gate signals are produced by the PWM technique to fire the switches of the inverter, which will be analyzed in detail in the following part (see Section IV-C).

A. Calculation of 0_1– and 0_2–Axis Reference Currents

According to the connection of neutral points of machine, the calculation of 0_1- and 0_2-axes reference currents can be divided into four cases.

1) Both 0_1- and 0_2-axes reference currents ($I_{01\_1}^*$ and $I_{02\_1}^*$) are equal to 0 when no source is connected to machine neutral points.
2) During the dc grid connection, the 0_1-axis reference current ($I_{01\_1}^*$) is set to 0 and the 0_2-axis ($I_{02\_2}^*$) is obtained by the charging controller, which is executed by two PI controllers connected in series. The first PI controller is employed to track the desired charging current I_b^* and generate the reference value of charging voltage, and the second one is used to regulate charging voltage V_b and produce 0_2-axis current reference.
3) If the VRPPs are connected, in addition to charging control, the MPPT of VRPPs is implemented by an adaptive perturb and observe (P&O) MPPT control [26]. In this scenario, the 0_1-axis reference current ($I_{01\_1}^*$) is still 0 and the minimum of charging control and MPPT output values ($I_{02\_2}^*$ and I_{PP}^*) is chosen as the 0_2-axis current reference ($I_{02\_3}^*$).
4) While the MEI-EDROC is fed by the single-phase grid, power factor correction (PFC) is applied to ensure unity power factor operation on the grid side. At first, the single-phase voltage position θ is found by a phase-locked loop (PLL) based on the second-order generalized integrator (SOGI) [11]. Then, the product of the charging control output value ($I_{02\_2}^*$) and sine of θ is used as the 0_1-axis reference current ($I_{01\_2}^*$). Different from last the two cases, the 0_2-axis current reference is 0 in this situation.

B. Mode Selection

Mode selection is designed according to the values of V_{DC}, V_{PP}, and V_{AC}, and there are four modes.

1) When all of V_{DC}, V_{PP}, and the rms value of V_{AC} are smaller than their thresholds V_{DCT}, V_{PPT}, and V_{ACrT}, mode $= 1$ ($I_{01}^* = I_{01\_1}^* = 0$ and $I_{02}^* = I_{02\_1}^* = 0$) and no mode switch is closed.
2) If the V_{DC} is larger than V_{DCT}, mode $= 2$($I_{01}^* = I_{01\_1}^* = 0$ and $I_{02}^* = I_{02\_2}^*$) and S_2 is in ON.
3) When only V_{PP} is greater than V_{PPT}, mode $= 3$($I_{01}^* = I_{01\_1}^* = 0$ and $I_{02}^* = I_{02\_3}^*$) and S_1 is in ON.
4) If the rms value of V_{AC} is larger than V_{ACrT}, mode $= 4$($I_{01}^* = I_{01\_2}$ and $I_{02}^* = I_{02\_1}^* = 0$) and S_3 is in ON.

C. Synchronous and 120° Interleaving PWM Schemes

In order to generate the gate signals of the inverter, synchronous and 120° interleaving PWM schemes are applied, respectively, for different control objectives. In the synchronous PWM modulation, all the six modulating waves $V_A^* \sim V_W^*$ share a common carrier wave and the six driving signals can be simultaneously of high level or low level. According to the definition of the common-mode voltages on the 0_1-axis and 0_2-axis [27], as indicated in (12), the 0_1-axis common-mode voltage (V_{01}) is zero when the driving signals are either all high or low. In other cases, V_{01} alters between $-1/2V_b$ and $1/2V_b$. Therefore, the fluctuation range of V_{01} is small, with a predominant occurrence of zero, as illustrated in Fig. 13(a). However, the variation range of the 0_2-axis common-mode voltage (V_{02}) is either 0 or V_b.

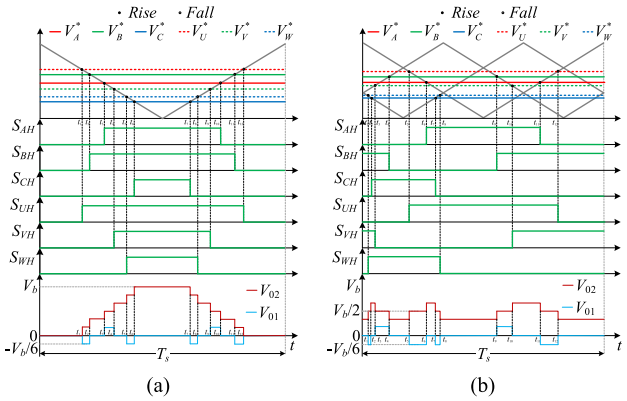

Fig. 13. Gate signals and 0_1- and 0_2-axes voltages. (a) Synchronous PWM scheme. (b) 120° interleaving PWM scheme.

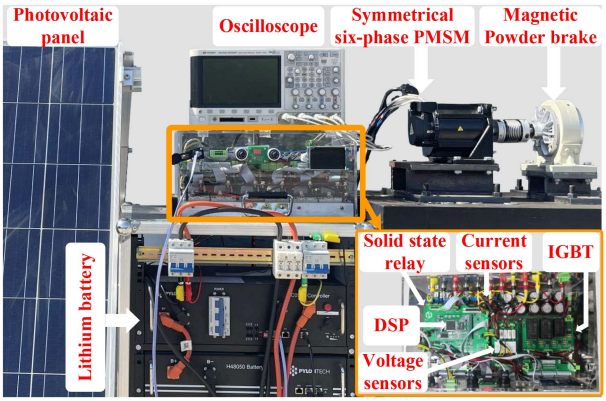

Fig. 14. Experimental prototype.

Using the synchronous PWM scheme will cause a large 0_2-axis voltage fluctuation, resulting in a considerable 0_2-axis current ripple in the in-motion charging mode.

In contrast, three carrier waves that are out of phase by one-third of a switching period are used in the 120° interleaving PWM scheme. According to (12), the 0_2-axis voltage fluctuation can be significantly reduced due to the cancellation effect, as shown in Fig. 13(b). Additionally, it can be observed that the fluctuation range of V_{01} is still small.

$$\begin{cases} V_{01} = \frac{1}{6}\left(V_A + V_B + V_C - V_U - V_V - V_W\right) \\ V_{02} = \frac{1}{6}\left(V_A + V_B + V_C + V_U + V_V + V_W\right). \end{cases} \tag{12}$$

V. Experimental Verifications

In order to validate the feasibility and effectiveness of the proposed MEI-EDROC, an experimental test rig with the rated power of 2 kW is conducted as shown in Fig. 14. A 2-kW six-phase symmetrical PMSM is employed and the main parameters of the machine are listed in Table II. The load is produced by a magnetic powder brake. Two 36 V/300 W VRPPs connected in series, a dc power supply with a maximum voltage of 100 V and an ac power source are chosen to imitate the VRPPs, the emerging dc grid, and the single-phase grid, respectively. The battery under test is with 144 V/50 AH. A multifunctional onboard charger is made, where six Infineon FF300R12ME4

TABLE II
Main Parameters of the Symmetrical Six-Phase PMSM

Parameters	Values
Rated power	2.0 kW
Rated speed	2000 r/m
Number of pole pairs	5
Direct axis inductance	5.56 mH
Quadrature axis inductance	7 mH
0-axis inductance	0.125 mH
Phase resistance	0.3Ω
Stator-PM magnetic flux	0.042 Wb

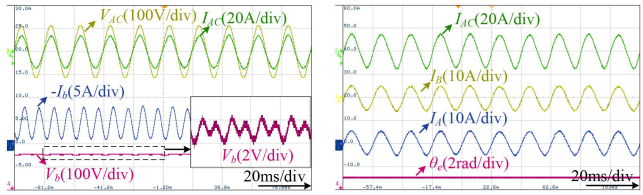

Fig. 15. Single-phase charging performances.

IGBT modules are used to constitute the six-phase inverter. Due to the limitation of the experimental platform, the operating frequency of the IGBTs in this system is 10 kHz, which can satisfy all modes. In addition, with regard to the current and voltage measurement, HCS-LTS3-15A current sensors and HVS-AS3.3-05 mA voltage sensors are used. Furthermore, the proposed ICS is achieved by a TMS320F28335 digital controller board.

A. Single-Phase Charging and DC Charging

First, the single-phase charging performances are evaluated considering the input voltage of 80 V. It can be observed from Fig. 15 that the phase shift between input voltage $V_{\rm AC}$ and input current $I_{\rm AC}$ is negligible, which indicates the unit power factor operation. The charging voltage V_b is about 150 V and its ripple is roughly 2 V. The charging current I_b is around 5 A and the second-order ripple current of 4 A can be noted due to the presence of second-order power pulsation on the input side. In addition, as shown in Fig. 15, the machine phase currents I_A and I_B are equal to one-third of $I_{\rm AC}$, generating zero electromagnetic torque. In other words, the rotor electrical angle maintains a constant value in this mode. Then, the experimental results of dc charging are illustrated in Figs. 16–18, where the dc power supply is set to 90 V and the VRPPs are operated in 1000 W/m^2 and 20 °C. Fig. 16 shows the steady-state experimental waveforms of the dc charging mode for the 120° interleaving and the synchronous PWM schemes, where the dc power supply is used. The charging current I_b (approximately 8 A) tracks its set value, with a constant charging voltage V_b (approximately 150 V) observed, which meets the basic requirements of battery charging. The ripple of the current outputted from the dc power supply ($I_{\rm DC}$) for the 120° interleaving PWM scheme (approximately 1.5 A) is lower than that obtained by the synchronous PWM scheme (approximately 5 A), owing to the cancellation effect. However, due to a larger equivalent inductance of machine winding (which is changed with the magnetic conductivity), the ripple of machine phase current

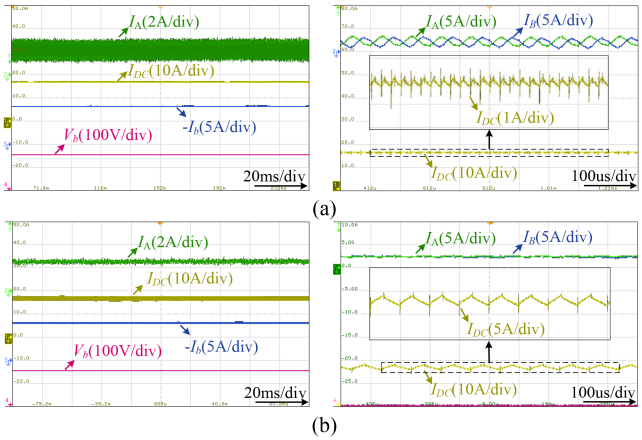

Fig. 16. DC charging operation performances powered by DC source in steady state. (a) With 120° interleaving PWM scheme. (b) With synchronous PWM scheme.

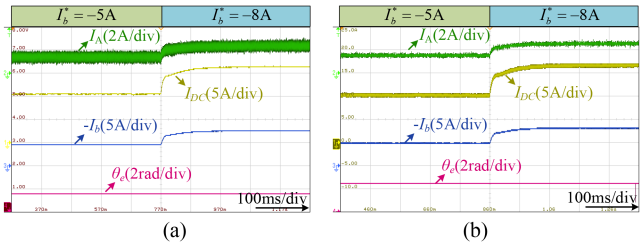

Fig. 17. DC charging performances powered by DC source to a step in charging current from 5 to 8 A. (a) With 120° interleaving PWM scheme. (b) With synchronous PWM scheme.

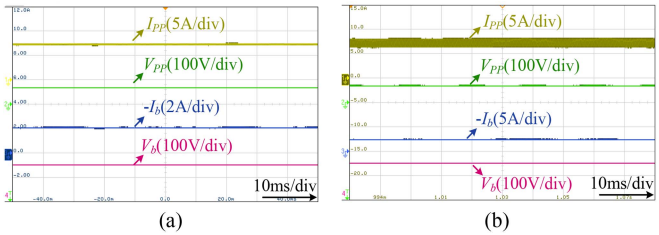

Fig. 18. DC charging operation performances powered by the VRPPs in steady state. (a) With 120° interleaving PWM scheme. (b) With synchronous PWM scheme.

for the synchronous PWM scheme is lower. In addition, the machine phase currents are the same, which means that zero electromagnetic torque is generated. Thus, it can be observed from Fig. 17 that the rotor electrical angle is unvaried during dc charging. Meanwhile, excellent charging current-tracking performance can be observed when the charging current is varied in a step manner from 5 to 8 A, as shown in Fig. 17. The experiment results of dc charging powered by the VRPPs are presented in Fig. 18. Obviously, the charging current I_b and voltage V_b both remain constant. Although the output current (I_{PP}) ripple of the VRPPs for the synchronous PWM scheme is obviously larger than one for the 120° interleaving PWM scheme, the difference

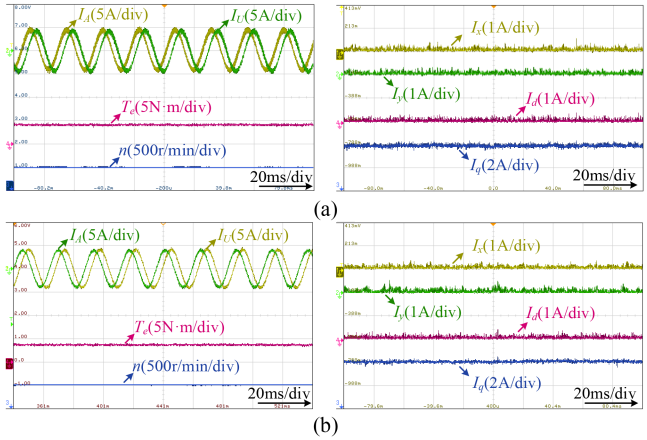

Fig. 19. Normal driving performances. (a) With 120° interleaving PWM scheme. (b) With synchronous PWM scheme.

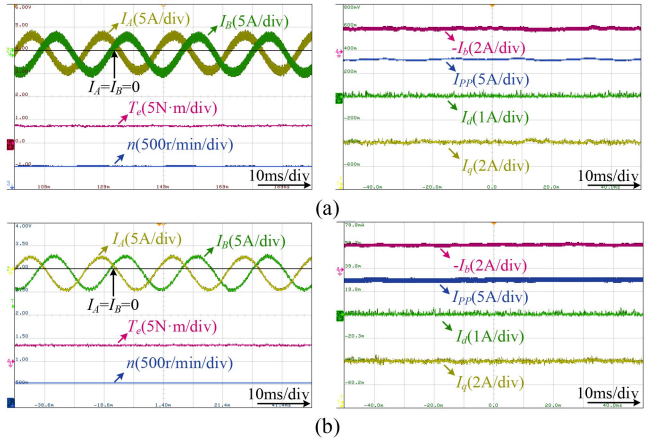

Fig. 20. In-motion charging performances in steady state. (a) With 120° interleaving PWM scheme. (b) With synchronous PWM scheme.

of the VRPPs voltages V_{PP} can be ignored since the VRPPs are in parallel with a 4700-μF electrolytic capacitor.

B. Normal Driving and in-Motion Charging

Fig. 19 depicts the steady-state performance of the normal driving mode under the desired speed of 500 r/min in conjunction with 4 N·m load. It can be found that the machine phase currents are extremely sinusoidal for two PWM schemes. Although the ripple of the machine phase current is larger for the 120° interleaving PWM scheme, the ripples of d–q, and x–y subspace currents (I_d, I_q, I_x, and I_y) are the same for the two PWM schemes. Besides, the speed n and the output torque T_e of the machine are constant for two PWM schemes.

Then, the performances of in-motion charging are evaluated when the VRPPs are in the condition of 1050 W/m^2 and 20 °C. Fig. 20 illustrates the steady-state performance where the speed is set to 500 r/min and the magnetic powder brake output is set to 4 N·m. It can be observed that the phase currents are sinusoidal with a bias current of −1.2 A due to the imposed 0_2-axis current. Meanwhile, the d–q subspace currents, the speed and the output

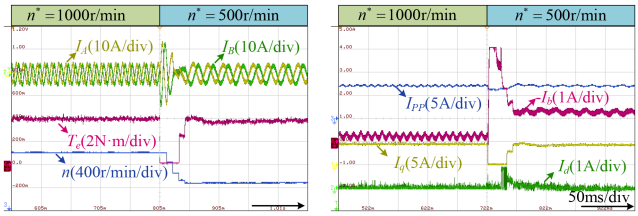

Fig. 21. In-motion charging dynamic performances under a step of speed from 1000 to 500 r/min.

torque of the machine are constant for these two PWM schemes. Compared with the synchronous PWM scheme, the ripple of machine phase current is larger for the 120° interleaving PWM scheme, but the ripple of the VRPPs output current is lower. In addition, the output current of the battery is approximately −2A, which means the battery is under charging.

Also, in order to analyze the dynamic performances in the in-motion charging, incorporating 120° interleaving PWM scheme, the experiment under the condition of speed step-change from 1000 to 500 r/min is carried out, as shown in Fig. 21. Owing to the decoupling between 0_2-axis and the d–q subspace components, the output current (I_{PP}), and hence, the output power of the VRPPs remain the same from beginning to end. Besides, both I_d and I_q maintain the same values under constant torque conditions. In addition, a satisfactory dynamic performance (rough 70 ms) can be observed. It should also be noticed that the charging current increases under the final steady state because the energy consumption for driving is decreased by reducing speed manners.

Moreover, the FFT results of I_A in the normal driving mode are depicted in Fig. 23. The total harmonic distortion (THD) of phase current in the normal driving mode with 120° interleaving PWM scheme is about 5.14%, which is higher than that with synchronous PWM scheme (2.88%). This distinction is primarily attributed to the larger equivalent inductance of the machine winding, which varies in accordance with magnetic conductivity, prevailing in the synchronous PWM scheme. Additionally, the FFT results of I_A in the in-motion charging mode are depicted in Fig. 24. The THD of phase current in the in-motion charging mode with 120° interleaving PWM scheme is about 7.42%, which is higher than that with the synchronous PWM scheme (7.10%). In contrast to the normal driving mode, the harmonic increases significantly in the in-motion charging mode as a result of the unequal impedances of stator windings and composition of zero-sequence space.

C. Mode Switching

The performances of mode switching are evaluated in combination with the 120° interleaving PWM scheme. Fig. 22(a) exhibits the experiment results of mode switching from in-motion charging to dc charging. It can be noted that the speed drops rapidly to zero. Because a magnetic powder brake is employed as load, a constant braking torque always exists during the mode switching. Thus, the output torque and the q-axis

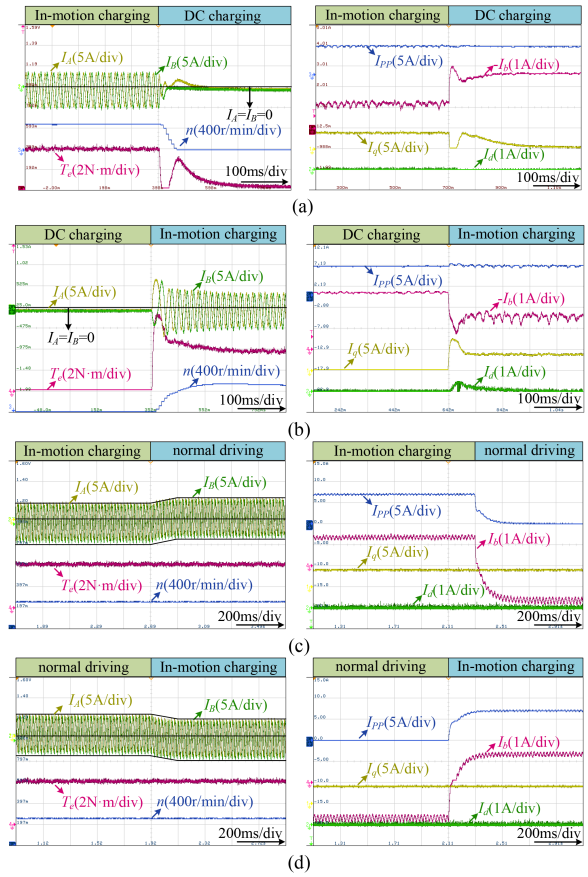

Fig. 22. Mode switching performances. (a) From in-motion charging to DC charging. (b) From DC charging to in-motion charging. (c) From in-motion charging to normal driving. (d) From normal driving to in-motion charging.

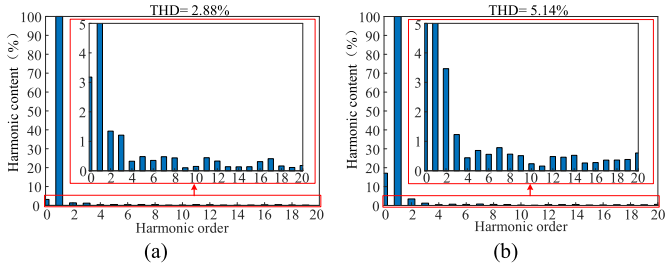

Fig. 23. THD of I_A in normal driving mode under speed setting of 500 r/min with 4 N·m load. (a) With synchronous PWM scheme. (b) With 120° interleaving PWM scheme.

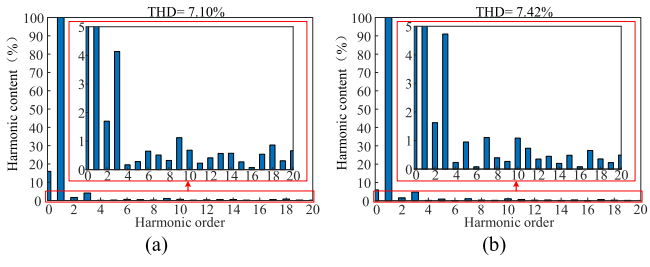

Fig. 24. THD of I_A in in-motion charging mode under speed setting of 500 r/min with 4 N·m load. (a) With synchronous PWM scheme. (b) With 120° interleaving PWM scheme.

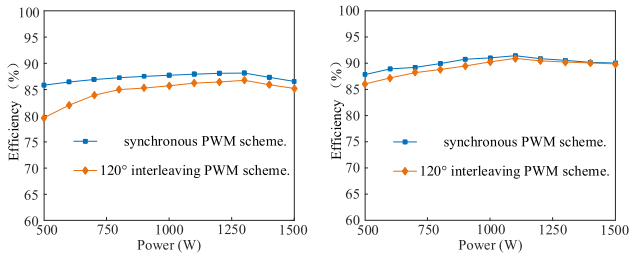

Fig. 25. Efficiency results of the studied MEI-EDROC system. (a) DC charging mode. (b) In-motion charging mode.

current are not equal to zero, causing differences in machine phase currents. Then, the mode switching from dc charging to in-motion charging is conducted, as presented in Fig. 22(b). The speed n is quickly adjusted to its given value (500 r/min). In addition, it can be found from Fig. 22(a) and (b) that the VRPPs output current remains constant during mode switching between in-motion charging and dc charging. Finally, the experiments for mode switching between normal driving and in-motion charging are implemented, as illustrated in Fig. 22(c) and (d). Due to the decoupling of between 0_2-axis and d–q subspace components, it can be seen that the d–q subspace currents, and hence, the speed and the output torque are unchanged for both cases, which satisfies the theoretical analyses in Section III.

D. Efficiency Discussion

The efficiency of the MEI-EDROC system in single-phase charging mode is 88.23% under the input voltage of 80 V. Due to the presence of second-order power fluctuations on the input side, there is a significant second-order ripple current in the battery measurement.

The efficiency of the MEI-EDROC system in the dc charging mode with different schemes is evaluated by manually adjusting the input current by regulating the charging current, which is in a range of 5–15 A. Considering the input voltage is approximately constant at 100 V, the power roughly ranges from 500 to 1500 W. The efficiency curve is presented in Fig. 25(a). Generally, the efficiency increases with the charging power. In particular, the peak efficiency achieved at 1300 W input power is up to 88.14% with synchronous PWM scheme and 86.75% with 120° interleaving PWM scheme, which is lower than traditional on-board charger (over 94%). There are two main reasons restricting charging efficiency. On the one hand, the utilization of machine windings as the filters would lead to higher resistances in comparison to the customized filters in dedicated chargers, which is the primary contributor to power loss. On the other hand, applying high-rated power switching devices and six-phase PMSM without optimization to a low-rated laboratory prototype would lead to higher motor losses [9]. Currently, relevant investigations have been conducted regarding the issue of charging efficiency. Concretely, optimizing the power switching devices, specifically the utilization of wide bandgap semiconductor technologies like SiC, is a viable approach to enhancing charging efficiency [17].

For in-motion charging mode, in order to obtain its efficiency curve, the dc source instead of the VRPPs is connected between the machine natural points and the battery negative to flexibly adjust input power. The input power from the dc source ranges from 500 to 1500 W. The efficiency curve with different schemes is drawn in Fig. 25(b). It can be observed that the efficiency increases with the input power. The peak efficiency is 91.43% at 1100 W input power with a synchronous PWM scheme and the other peak efficiency is 90.93% with 120° interleaving PWM scheme at the same input power.

The efficiency of different PWM schemes shown in Fig. 25 illustrates the efficiency with the synchronous PWM scheme is higher than that with the 120° interleaving PWM scheme under the same input power. In principle, the 0_2-axis voltage fluctuation increases with the synchronous PWM scheme, but the ripple of machine phase current is low, which results in lower loss in normal driving and in-motion charging mode. In contrast, due to the cancellation effect, 0_2-axis voltage fluctuation can be significantly reduced by 120° interleaving PWM scheme, which can ameliorate charging quality. However, it is noted that the machine phase ripple current is larger, which increases machine losses. Henceforth, in specific designs, practical factors need to be comprehensively considered, and the appropriate PWM scheme should be chosen based on actual circumstances in order to accomplish preferable system performance.

VI. Conclusion

In the article, the MEI-EDROC with the ability of dc charging, single-phase charging, in-motion charging, and normal driving for SPEV incorporating a six-phase machine is studied. Circuit topology, switching conditions of four operation modes and operation principles, especially the in-motion charging mode, of the MEI-EDROC are discussed in detail. After that, by extending the vector control strategy of six-phase machine driving, the ICS responsible for all operation modes is proposed, which makes the system control simpler and more reliable. Finally, the MEI-EDROC system with the ICS is successfully verified by a 2-kW experimental prototype. According to the experiment results, the following conclusions are obtained.

1) By the ICS, dc charging, single-phase charging, in-motion charging, and normal driving can be successfully implemented.
2) In dc charging and in-motion charging, compared with synchronous PWM scheme, the ripple of the VRPPs or the dc power supply output current (or 0_2-axis current) for 120° interleaving PWM scheme is smaller, but the machine phase current is larger.
3) In in-motion charging, the VRPPs output power is invariant by changes in speed due to the decoupling between the 0_2-axis and the d–q subspace components. In addition, the dedicated dc–dc converter between the VRPPs and the battery is eliminated in in-motion charging mode and dc charging mode.
4) During the mode switching between in-motion charging and dc charging, the VRPPs output power is constant. In addition, the mode switching between in-motion charging and normal driving has no impact on the EV driving performances.

REFERENCES

[1] M. Tong, M. Cheng, S. Wang, and W. Hua, "An on-board two-stage integrated fast battery charger for EVs based on a five-phase hybrid-excitation flux-switching machine," *IEEE Trans. Ind. Electron.*, vol. 68, no. 2, pp. 1780–1790, Feb. 2021.

[2] C. Viana, M. Pathmanathan, and P. W. Lehn, "Dual-inverter-integrated three-phase EV charger based on split-phase machine," *IEEE Trans. Power Electron.*, vol. 37, no. 12, pp. 15175–15185, Dec. 2022.

[3] S. Q. Ali, D. Mascarella, G. Joos, and L. Tan, "Torque cancelation of integrated battery charger based on six-phase permanent magnet synchronous motor drives for electric vehicles," *IEEE Trans. Transp. Electrific.*, vol. 4, no. 2, pp. 344–354, Jun. 2018.

[4] H. J. Raherimihaja, Q. Zhang, T. Na, M. Shao, and J. Wang, "A three-phase integrated battery charger for EVs based on six-phase open-end winding machine," *IEEE Trans. Power Electron.*, vol. 35, no. 11, pp. 12122–12132, Nov. 2020.

[5] D. Thimmesch, "An SCR inverter with an integral battery charger for electric vehicles," *IEEE Trans. Ind. Appl.*, vol. IA-21, no. 4, pp. 1023–1029, Jul. 1985.

[6] J. Cai and X. Zhao, "An on-board charger integrated power converter for EV switched reluctance motor drives," *IEEE Trans. Ind. Electron.*, vol. 68, no. 5, pp. 3683–3692, May 2021.

[7] Y. Zhang, J. Fang, F. Gao, T. Song, S. Gao, and D. J. Rogers, "Second-harmonic ripple voltage suppression of integrated single-phase pulse width modulation rectifier charging system for EVs," *IEEE Trans. Power Electron.*, vol. 35, no. 4, pp. 3616–3626, Apr. 2020.

[8] A. Salem and M. Narimani, "A review on multiphase drives for automotive traction applications," *IEEE Trans. Transp. Electrific.*, vol. 5, no. 4, pp. 1329–1348, Dec. 2019.

[9] X. Liu, F. Yu, J. Mao, and H. Yang, "Pre- and post-fault operations of six-phase electric-drive-reconstructed onboard charger for electric vehicles," *IEEE Trans. Transp. Electrific.*, vol. 8, no. 2, pp. 1981–1993, Jun. 2022.

[10] M. S. Abdel-Majeed et al., "A three-phase nonisolated pseudo-six-phase-based integrated onboard battery charger for electric vehicles," *IEEE Trans. Transp. Electrific.*, vol. 9, no. 1, pp. 1300–1310, Mar. 2023.

[11] M. Tong, M. Cheng, W. Hua, and S. Ding, "A single-phase on-board two-stage integrated battery charger for EVs based on a five-phase hybrid-excitation flux-switching machine," *IEEE Trans. Veh. Technol.*, vol. 69, no. 4, pp. 3793–3804, Apr. 2020.

[12] F. Yu, W. Zhang, Y. Shen, and J. Mao, "A nine-phase permanent magnet electric-drive-reconstructed onboard charger for electric vehicle," *IEEE Trans. Energy Convers.*, vol. 33, no. 4, pp. 2091–2101, Dec. 2018.

[13] Y. Xiao and C. Liu, "A study of rotational movement and charging torque of reconfigured on-board charger," *IEEE Trans. Power Electron.*, vol. 35, no. 10, pp. 10720–10728, Oct. 2020.

[14] Y. Xiao, C. Liu, and F. Yu, "An effective charging-torque elimination method for six-phase integrated on-board EV chargers," *IEEE Trans. Power Electron.*, vol. 35, no. 3, pp. 2776–2786, Mar. 2020.

[15] S. He, Z. Xu, M. Chen, H. Yang, and W. Li, "General derivation law with torque-free achieving of integral on-board charger on compact powertrains," *IEEE Trans. Ind. Electron.*, vol. 68, no. 2, pp. 1791–1802, Feb. 2021.

[16] Y. Xiao, C. Liu, and F. Yu, "An integrated on-board EV charger with safe charging operation for three-phase IPM motor," *IEEE Trans. Ind. Electron.*, vol. 66, no. 10, pp. 7551–7560, Oct. 2019.

[17] E. Hoevenaars and M. Hiller, "Conceptualization and efficiency review of integrated chargers using six-phase machines," *IEEE Trans. Transp. Electrific.*, vol. 8, no. 1, pp. 48–61, Mar. 2022.

[18] M. S. Abdel-Majeed et al., "Postfault operation of onboard integrated battery charger via a nine-phase EV-drive train," *IEEE Trans. Ind. Electron.*, vol. 68, no. 7, pp. 5626–5637, Jul. 2021.

[19] A. K. Singh, M. Badoni, and Y. N. Tatte, "A multifunctional solar PV and grid based on-board converter for electric vehicles," *IEEE Trans. Veh. Technol.*, vol. 69, no. 4, pp. 3717–3727, Apr. 2020.

[20] B. Wang, X. Zhang, U. Manandhar, H. B. Gooi, Y. Liu, and X. Tan, "Bidirectional three-level cascaded converter with deadbeat control for HESS in solar-assisted electric vehicles," *IEEE Trans. Transp. Electrific.*, vol. 5, no. 4, pp. 1190–1201, Dec. 2019.

[21] "Lightyear one. Designed for independence," *Lightyear*, 2021. Accessed: Nov. 9, 2021. [Online]. Available: https://lightyear.one/lightyear-one

[22] C. Viana and P. W. Lehn, "A drivetrain integrated DC fast charger with buck and boost functionality and simultaneous drive/charge capability," *IEEE Trans. Transp. Electrific.*, vol. 5, no. 4, pp. 903–911, Dec. 2019.

[23] F. Yu, Z. Zhu, X. Liu, and Z. Zhang, "Electric-drive-reconstructed on-board charger for solar-powered electric vehicles incorporating six-phase machine," *IEEE Trans. Power Electron.*, vol. 37, no. 6, pp. 6544–6555, Jun. 2022.

[24] Y. Hu, C. Gan, W. Cao, Y. Fang, S. J. Finney, and J. Wu, "Solar PV-powered SRM drive for EVs with flexible energy control functions," *IEEE Trans. Ind. Appl.*, vol. 52, no. 4, pp. 3357–3366, Jul./Aug. 2016.

[25] A. Al-Haj Hussein and I. Batarseh, "A review of charging algorithms for nickel and lithium battery chargers," *IEEE Trans. Veh. Technol.*, vol. 60, no. 3, pp. 830–838, Mar. 2011.

[26] A. K. Abdelsalam, A. M. Massoud, S. Ahmed, and P. N. Enjeti, "High-performance adaptive perturb and observe MPPT technique for photovoltaic-based microgrids," *IEEE Trans. Power Electron.*, vol. 26, no. 4, pp. 1010–1021, Apr. 2011.

[27] M. A. Waghmare, B. S. Umre, M. V. Aware, A. Kumar, and S. A. Yerkal, "Common-mode voltage minimization in three-phase to six-phase indirect matrix converter using virtual vector synthesization," *IEEE Trans. Ind. Appl.*, vol. 58, no. 4, pp. 4848–4858, Jul./Aug. 2022.

Feng Yu (Member, IEEE) was born in Suzhou, China, in 1985. He received the B.Eng. degree in electrical engineering and automation from the School of Electrical Engineering, Sanjiang University, Nanjing, China, in 2008, the M.Sc. degree in electrical engineering from the School of Electrical and Information Engineering, Jiangsu University, Zhenjiang, China, in 2011, and the Ph.D. degree in the electrical engineering in the Department of Electrical Engineering, Southeast University, Nanjing, in 2016.

Since 2016, he has been with Nantong University, Nantong, China, where he is currently a Professor with the School of Electrical Engineering. His current research interests include the control of multiphase machines and drives for applications ranging from automotive to renewable energy.

Qihao Yin was born in Xuzhou, China, in 2000. He received the B.Eng. degree in electrical engineering and automation in 2022 from the School of Electrical Engineering, Nantong University, Nantong, China, where he is currently working toward the M.Sc. degree in control science and engineering.

His main research interests include electric-drive-reconstructed onboard charging system along with multifunctional applications in solar electric vehicles.

Zhihao Zhu was born in Henan, China, in 1996. He received the B.Eng. degree in electrical engineering and automation and M.Eng. degree in control science and engineering from Nantong University, Nantong, China, in 2019 and 2022, respectively. He is currently working toward the Ph.D. degree in control science and engineering with Tianjin University, Tianjin, China.

His main research interests include control of multiphase drive systems, model predictive control of power electronics, and electric-drive-reconstructed onboard charger along with its application in electric vehicle.

Xunhui Cheng was born in Lu'an, China, in 2001. She received the B.Eng. degree in automation in 2022 from the School of Electrical Engineering, Nantong University, Nantong, China, where she is currently working toward the M.Sc. degree in control science and engineering with the School of Electrical Engineering, Nantong University, Nantong, China.

Her current research interests include power electronics and electric-drive-reutilized onboard charger along with its application in electric vehicle.